Title

Significant correlations between human cortical bone mineral density and quantitative susceptibility mapping (QSM) obtained with 3D Cones ultrashort echo time magnetic resonance imaging (UTE-MRI)

Authors

Jerban, Saeed
Lu, Xing
Jang, Hyungseok
et al.

Publication Date

2019-10-01

DOI

10.1016/j.mri.2019.06.016

Peer reviewed

Published in final edited form as:

Magn Reson Imaging. 2019 October ; 62: 104–110. doi:10.1016/j.mri.2019.06.016.

Significant correlations between human cortical bone mineral density and quantitative susceptibility mapping (QSM) obtained with 3D Cones ultrashort echo time magnetic resonance imaging (UTE-MRI)

Saeed Jerban[a,†], **Xing Lu**[a,b,†], **Hyungseok Jang**[a], **Yajun Ma**[a], **Behnam Namiranian**[a], **Nicole Le**[c], **Ying Li**[d], **Eric Y. Chang**[c,a], **Jiang Du**[a]

[a]Department of Radiology, University of California, San Diego, CA, USA

[b]12sigma Inc., San Diego, CA, USA

[c]Radiology Service, VA San Diego Healthcare System, San Diego, CA, USA

[d]First affiliated hospital of Zhengzhou University, Zhengzhou, Henan, China

Abstract

Purpose: Quantitative susceptibility mapping (QSM) MRI is a tool that can characterize changes in susceptibility, an intrinsic property which is associated with compositional changes in the tissue. Current QSM estimation of cortical bone is challenging because conventional clinical MRI cannot acquire signal in cortical bone. This study aimed to implement Cones 3D ultrashort echo time MRI (UTE-MRI) for *ex vivo* QSM measurements in human tibial cortical bone, investigating the correlations of QSM with volumetric intracortical bone mineral density (BMD).

Materials and Methods: Nine tibial midshaft cortical bone specimens (25 mm long specimens cut at the mid-point of tibial shaft, 67±20 years old, 5 women and 4 men) were scanned on a clinical 3T MRI scanner for QSM measurement. The specimens were also scanned on a high-resolution micro-computed tomography (μCT) scanner for volumetric BMD estimation. QSM and μCT results were compared at approximately nine regions of interest (ROIs) per specimen.

Results: Average 3D UTE-MRI QSM showed significantly strong correlation with volumetric BMD ($R=-0.82$, $P<0.01$) and bone porosity ($R=0.72$, $P<0.01$). Combining all data points together (77 ROIs), QSM showed significant moderate to strong correlation with volumetric BMD after correction for interdependencies in specimens ($R=-0.70$, $P<0.01$). The corrections were required

Corresponding authors: • **Jiang Du**, Department of Radiology, University of California, 9500 Gilman Dr., San Diego, CA 92093, USA , jiangdu@ucsd.edu , Phone: +1 858 246 2248, Fax: +1 888 960 5922, • **Saeed Jerban**, Department of Radiology, University of California, 9500 Gilman Dr., San Diego, CA 92093, USA, sjerban@ucsd.edu, Phone : +1 858 246 3158, Fax : +1 888 960 5922.
†These authors contributed equally to this work.

6. Conflict of interest statement

The authors have no conflicts of interest to declare.

because the data points were not independent in each specimen. Similarly, the correlation between QSM and porosity was significant (R=0.68, P<0.01).

Conclusions: These results suggest that the Cones 3D UTE-MRI QSM technique can potentially serve as a novel and accurate tool to assess intracortical bone mineral density whilst avoiding ionizing radiation.

Keywords

cortical bone; ultrashort echo time MRI; quantitative susceptibility mapping; bone mineral density

1. Introduction

Current cortical bone assessment focuses mainly on the mineral compartment of bone, measuring variation of bone mineral density (BMD) in patients by employing ionizing radiation-based techniques, such as dual-energy X-ray absorptiometry (DEXA) and quantitative computed tomography (QCT) [1,2]. Employing magnetic resonance imaging (MRI) for bone quality assessment has become of great interest due to the relatively safe nature of MRI compared with x-ray based techniques [1,3–6]. Moreover, providing MRI-based bone assessment will enable a comprehensive assessment of bone and surrounding soft tissues in one MRI session that significantly benefits both patients and physicians.

Among MRI techniques, quantitative susceptibility mapping (QSM) has recently received increased attention as a powerful tool to characterize pathophysiologic variation of magnetic susceptibility in tissues [7,8,17,9–16]. It is hypothesized that most diseases may affect tissue composition and chemical fractions. In bone tissue, any mineral variations caused by bone diseases may affect the magnetic susceptibility. QSM de-convolves magnetic susceptibility of the tissue based on the phase changes in the MR signal, where tissues with stronger magnetic susceptibility undergo faster evolution of phase [18,19]. Specifically for QSM calculation, gradient recalled echo (GRE) imaging is commonly performed, where MR images at multiple echo times (TEs) are typically acquired to measure the phase evolution accurately. Unfortunately, clinical MRI is not able to detect considerable signal of cortical bone for QSM applications because of bone's very short apparent transverse relaxation time (T2*) [1,3–5].

Strong correlations between QSM and BMD in trabecular bone of spine or ankle have been reported with the use of clinical MRI sequences [20,21]. Since clinical MRI is not capable of imaging bone with considerable signal, Dimov et al. [6] developed the 3D radial ultrashort echo time (UTE)-MRI QSM technique for potential detection of BMD variation in porcine hoof and human distal femur. The capability of UTE-MRI for quantitative bone imaging has been discussed by various research groups [22,23,32,33,24–31]. More specifically, UTE-MRI can acquire signal several microseconds after radiofrequency (RF) excitation before the rapid transverse magnetization decay of cortical bone [3,4].

Dimov et al. [6] reported significant correlations between computed tomography (CT) Hounsfield unit and radial 3D UTE-MRI QSM values in a combined set of ROIs covering tendon, trabecular bone, and cortical bone. Cones 3D UTE-MRI imaging [34–36] has

recently emerged as a way to achieve a faster acquisition speed compared with the radial 3D UTE-MRI techniques. Cones 3D UTE-MRI generally utilizes a short rectangular excitation pulse followed by an efficient spiral trajectory data readout with a minimal nominal TE of 32 μs (a minimal TE of 8 μs can be achieved with the addition of a fast transmit/receive switch) [34–36]. The Cones trajectories are more time-efficient than radial trajectories in covering 3D k-space [37] and resolve the limitations associated with 2D UTE sequences, namely, sensitivity to eddy currents[38]. Furthermore, the 3D UTE Cones sequence allows anisotropic fields of view (FOVs) and spatial resolution, resulting in vastly reduced scan times[39–41]. Lu et al. [42] combined the Cones 3D UTE-MRI and QSM techniques to detect the variation of iron concentration in phantoms. Later, Lu et al. [43] showed that the Cones 3D UTE-MRI technique results in similar QSM values, but faster scanning process, compared with radial 3D UTE-MRI technique. Jang et al. [44] demonstrated that Cones 3D UTE-MRI and 3D single point UTE-MRI QSM measurements are feasible in cortical bone specimens. However, the correlation of Cones 3D UTE-MRI QSM and BMD in cortical bone has not been investigated. Such *ex vivo* correlation studies are required before investigating the clinical utility of Cones 3D UTE-MRI QSM for *in vivo* cortical bone assessment.

This study aimed to determine the correlations of 3D Cones UTE-MRI QSM with μCT-based volumetric BMD and bone porosity in human cortical bone specimens. This study complements earlier feasibility studies and provides additional understanding of the technique's sensitivity before translation of the 3D Cones UTE-MRI QSM method to clinical *in vivo* studies.

2. Materials and methods

2.1. Sample preparation

Nine cortical bone specimens were harvested from freshly frozen human tibial midshafts (67±20 years old, 5 women and 4 men). These tibial midshafts were provided by a nonprofit whole-body donation company (United Tissue Network, Phoenix, AZ). Bone specimens were cut to 25 mm in length roughly at the mid-point of the tibial shaft using a Delta ShopMaster band saw (Delta Machinery, Tennessee, USA), then immersed in phosphate-buffered saline (PBS) for four hours at room temperature before the MRI scans. Loose marrow which was not trapped in pores was removed with a scalpel. The bone samples were embedded in 1% weight/volume agarose gel in a cylindrical plastic container (160 mm diameter and 200 mm length). Bone samples were scanned in 3 groups (2, 3, and 4 specimens in each container).

2.2. UTE-MR protocol

The UTE-MRI scans were performed on a 3T clinical scanner (MR750, GE Healthcare Technologies, Waukesha, WI) using an eight-channel knee coil for both RF transmission and signal reception. The UTE- MRI scans involved six Cones 3D UTE-MRI sequences with the following TEs: 0.032, 0.2, 0.4, 1.2, 1.8, 2.4 ms. Details of the Cones 3D UTE sequence are given in previous studies [34–36]. Other scanning parameters were as follows: sampling

bandwidth (BW)=83.3 kHz, flip angle=10°, TR=30 ms, matrix size=256×256×30, voxel size=0.5×0.5×2 mm^3.

Each Cones 3D UTE acquisition was reconstructed into both magnitude and phase images using a re-gridding algorithm, which interpolates the measured signal from Cones spokes onto a Cartesian grid. Nominal TEs were used for QSM calculation. Due to the non-uniform sampling density in 3D Cones trajectory (spiral trajectory on conical surfaces), density compensation was applied to the measured signal prior to re-gridding. The six single echo MRI acquisitions were combined to form a 4D complex matrix with an increasing order of TEs.

For the calculation of susceptibilities in bone specimens, a chemical shift species-specific R2* signal model-based UTE QSM (CSSR UTE QSM) reconstruction was applied offline on the generated 4D UTE matrix [6]. The region outside of the cylindrical phantom container (i.e., air) was masked out from the 4D UTE matrix. The B_0 direction was calculated from localization information in the MRI dataset and as the input for the QSM reconstruction protocol. The first three echoes of each dataset (TE=0.032, 0.2, and 0.4 ms) were used for estimating frequency shift in an iterative fashion. Specifically, the phase wrapping phenomena at the three first TEs were negligible. Then, a region growing-based phase unwrapping algorithm [45] was implemented to obtain the global frequency shift (f0).

Better frequency shift map (fm) and R2* were estimated using a graph-cut-based iterative decomposition of water and fat with echo symmetry and least-squares estimation (IDEAL)-based algorithm at each slice of the data[46–48]. Then, the corrected frequency shift map (f_correct) map was obtained by fitting the complex 4D UTE matrix to a species-specific R2* signal model-based iterative least squares estimation with a multi-peak model [6]. Specifically, the Projection onto Dipole Fields (PDF) algorithm was used to remove the background from the corrected frequency shift map and mask [49]. Then, dipole inversion of the local susceptibility distribution was achieved using an iterative Bayesian regulation method [18]. For all datasets, the regularization parameter and the radius for the spherical mean value operator were set as 500 and 5, respectively, for calculating the QSM map. The steps of QSM measurement process are shown as a flowchart in Figure 1.

The average QSM values were calculated in one slice (2mm thick) at the middle of the specimens within nine regions of interest (ROIs) per specimen. ROIs were selected at different cortical bone layers and anatomical sites on the UTE images to provide an adequate range of BMD. Figure 2 illustrates the schematics of selected ROIs in one representative bone specimen. ROIs were drawn in four different bone sites: anterior, mid-lateral, mid-medial, and posterior.

2.3. Micro-computed tomography (μCT)

To measure volumetric bone mineral density (BMD), all bone specimens were taken out of the agarose gel and scanned using a Skyscan 1076 (Kontich, Belgium) μCT scanner at 9 μm isotropic voxel size. Specimens were scanned in the presence of two hydroxyapatite phantoms (0.25 and 0.5 gr/cm^3), which enabled deriving a linear function of image gray level to volumetric BMD values in bone specimens. Other scanning parameters were as

follows: a 0.05 mm aluminum plus a 0.038 mm copper filter, 100 kV, 100 mA, 0.4° rotation step, 5 frame-averaging, and 5 h scan time.

A single gray level threshold was used for μCT image segmentation of the bone voxels from void voxels or pores. The gray level threshold was selected for each set of μCT data by investigating the gray level histograms and pore interfaces in raw images. Thresholding resulted in a stack of binary images which were used only for porosity assessment. A local volumetric BMD value was calculated for each voxel of the μCT raw images using a linear function of the voxel's gray level, which was determined based on gray levels of hydroxyapatite phantoms. The average volumetric BMD value was calculated using local BMD values of all voxels within the selected ROIs in 222 consecutive μCT slices which corresponded to a 2 mm MRI slice. Average bone porosity in each ROIs was the number of pore voxels to total voxels. Porosity pixel map corresponding to the middle MRI image of each specimen was generated by superimposing the 222 consecutive segmented (binarized) μCT images (i.e., sum of matrices divided by the number of slices). Affine image registration was used to propagate ROIs selected on UTE MRI images (Figure 2) onto the μCT data. Image registration was performed manually by an image processing expert in MATLAB by selecting four identical points in images from MRI and μCT. Regions affected by μCT ring artifact were excluded from the study.

2.4. Statistical analysis

Average and standard deviation of Cones 3D UTE-MRI QSM and μCT-based volumetric BMD and porosity values were calculated for each bone specimen. Pearson's correlations were calculated between average QSM values in specimens and their average μCT-based measures (volumetric BMD and porosity). Pearson's correlations were also calculated using all selected ROIs combined together to examine the capability of UTE-MRI QSM in detecting the differences of volumetric BMD regardless of intracortical bone location. Because of the variable-length repeated measurements per specimen, the significance levels for all correlations were assessed using non-parametric bootstrap (with resampling by specimen, 1000 replicates per analysis) to adjust for within-specimen dependence. To understand the independent impact of BMD on QSM measures, the correlation coefficient between QSM and BMD was also calculated by adjusting for porosity variations. All the data analyses were performed in MATLAB (version 2017, The Mathworks Inc., Natick, MA, USA). Statistical analyses were performed using a statistical programming language (R, version 3.2.5, R Development Core Team, Vienna, Austria).

3. Results

Magnitude images and phase images of three representative scanned bone specimens for different TEs are shown in Supplemental Figure 1 and Supplemental Figure 2, respectively. Figure 3a illustrates the Cones UTE-MRI QSM map for a representative tibial bone specimen (45-year-old female). Figure 3b shows one representative μCT slice of the same specimen scanned at 9 μm voxel size. The typical nine selected ROIs are shown schematically on the μCT slice, where they were propagated from drawn ROIs on UTE MRI through image registration process. Figures 2c and d illustrate the bone porosity and

volumetric BMD maps, respectively, for the same specimen. Local maxima in the QSM map qualitatively correspond to the regions of high BMD and low porosity in μCT-based maps.

The average and standard deviation of QSM, BMD, and bone porosity values for each of the nine studied bone specimens are presented in Table 1. Four ROIs affected by μCT ring artifact were excluded from all statistical measurements in this study.

Scatter plots and linear regressions of average UTE-MRI QSM values on average volumetric BMD and bone porosity are shown in Figures 3a and b, respectively. Average QSM showed significantly strong correlations with volumetric BMD ($R=-0.82$, $P<0.01$) and bone porosity ($R=0.72$, $P<0.01$).

Pearson's correlations, with 95% significant intervals, and p values between UTE-MRI QSM and μCT-based results (volumetric BMD and porosity) are presented in Table 2 considering all selected ROIs combined together. Correlation coefficients became lower when combining all data points together compared with correlations obtained using average values (Figure 4). QSM showed significant moderate to strong correlations with volumetric BMD ($R=-0.70$ [−0.80,−0.54], $P<0.01$). The correlation between QSM and porosity was significant and in a similar range ($R=0.68$, $P<0.01$). The correlation between QSM and BMD after adjusting for porosity variations was poor, but still significant ($P=-0.32$, $P<0.01$).

Scatter plots and linear regressions of UTE-MRI QSM values on volumetric BMD and bone porosity are shown in Figures 4a and b, respectively. As mentioned in Table 2, QSM demonstrated slightly higher correlations with volumetric BMD compared with bone porosity. Data points of different bone sites (Figure 2) are illustrated with markers where no obvious differences were found between bone sites. Scatter plot and linear regression of UTE-MRI QSM values on R2* is shown in Supplemental Figure 3 where the correlation was significant, but poor ($R=0.38$, $p<0.01$).

4. Discussion

This study was the first to investigate the correlations of 3D Cones UTE-MRI QSM with μCT-based volumetric BMD and bone porosity in human cortical bone specimens. This study complements earlier feasibility studies employing 3D Cones UTE-MRI QSM to assess volumetric BMD differences in human cortical bone.

Chen et al. [20] previously studied the QSM technique's capability in detecting QCT-derived volumetric BMD variation *in vivo* at trabecular bone regions of lumber vertebrae. They observed significant strong correlations between QSM and age, as well as between QSM and volumetric BMD. Diefenbach et al. [21] investigated QSM for measuring trabecular bone density in ankle using GRE-based sequences. They found a significant strong correlation between QSM and trabecular bone density. Additionally, Rochefort et al. [50] used a phantom-based validated QSM technique to assess the human forearm. They reported QSM values in soft-tissue, cortical bone, and bone marrow consistent with values in the literature.

Dimov et al. [6] proposed estimating bone QSM in porcine hoof and human distal femur based on acquired bone images using 3D radial UTE-MRI technique. They reported

significant correlations between computed tomography (CT) in Hounsfield units and QSM values within a combined set of ROIs covering tendon, trabecular bone, and cortical bone of porcine hoof. However, this QSM validation process for cortical BMD assessment was limited since they considered various tissues for correlation analysis. Lu et al. [42] used 3D Cones UTE-MRI [34–36] combined with a QSM technique to detect the variation of iron concentration in phantoms. Employing 3D Cones in UTE imaging has helped to reduce the scan time and also to decrease image artifacts, such as blurring, in cortical bone scans. It has also been shown that QSM values obtained from different sampling trajectories are similar with no significant differences [43].

The current study validated the capability of the 3D Cones UTE-MRI QSM technique to detect human cortical bone volumetric BMD differences *ex vivo*, particularly between specimens. The QSM measurement from UTE images was similar to previous studies [6,42,44]. For the nine studied human tibial cortical bone specimens, average QSM values demonstrated significantly strong correlations with average BMD and cortical porosity (Figure 4). Considering all analyzed ROIs in the nine studied specimens combined together, QSM values demonstrated significant moderate to strong correlations with BMD and cortical porosity (Table 2, Figure 5). Lower correlation coefficients for combined data sets might be due to minor image registration errors between two modalities or due to lower intraspecimen sensitivity of the QSM technique. These need to be investigated in future studies with a larger number of specimens or subjects. Since the μCT scans were performed in high resolution and with 9 μm voxel size, volumetric BMD was highly correlated with bone porosity. Therefore, the QSM correlation with porosity was in the range of QSM and BMD correlation, though lower. Correlation between QSM and BMD after adjusting for porosity variations was found to be lower ($R=-0.70$ versus $R=-0.32$), but still significant ($P<0.01$), indicating QSM as an independent predictor of BMD.

Results in this study suggest that the 3D Cones UTE-MRI QSM technique has the potential to be examined as a sensitive tool for diagnosing bone diseases which can detect mineral level changes in human cortical bone without exposing patients to ionizing radiation. However, a separate sensitivity study is required to understand the sensitivity level of the presented QSM technique. Bone stress injuries [51,52] may also lead to QSM variation due to microfractures, though this hypothesis requires a future well-designed investigation.

MRI-based cortical bone assessment has also been investigated with the use of other UTE-MRI techniques which investigate the water proton pools. Such UTE-MRI techniques include bi-component T2* fitting [53], tri-component T2* analysis through modeling the fat signal [54], dual-echo UTE imaging (i.e., porosity index) [22], direct pore water imaging after nulling bound water [55–57], T1-based decomposition of total water signal [33,58], and magnetization transfer (MT) techniques [51,59–61].

This study had several limitations. First, this study was performed on *ex vivo* cortical bone specimens where low bone marrow and no surrounding muscles were present. Future well-designed *in vivo* studies should examine if the correlations between the Cones 3D UTE-MRI QSM and volumetric BMD are still apparent. In addition to the impact of other tissues on bone signal *in vivo*, the difference between body and room temperatures may introduce

some MRI differences [62,63]. Additional cross-sectional *in vivo* studies are required to compare BMD and MRI-QSM between healthy volunteers and osteoporotic patients to clarify the relevance of QSM and osteoporosis. Moreover, future longitudinal *in vivo* studies are needed to assess sensitivity of the QSM technique to BMD variations in patients. Second, QSM correlations with BMD may not imply good correlation between QSM and mechanical properties of cortical bone, which is critical in evaluating patient fracture risk. A well-designed specimen study is required to investigate the correlations between QSM and bone mechanical properties measured using bending tests applied on cortical bone strips. Third, the total scan time for Cones 3D UTE-MRI QSM was around 20 minutes, which is more than the clinical MRI sequences. Additional investigations are required to accelerate the Cones 3D UTE-MRI QSM technique for clinical applications. This can be achieved by stretching the spiral trajectories, while reducing the number of readouts [64]. Fourth, nowadays, x-ray-based techniques are quite appropriate for BMD measurement at proximities with limited radiation dosage and at a low cost. However, peripheral MRI scanners may be available in the near future that result in affordable costs similar to those of HR-pQCTs. Moreover, other MRI techniques to assess water protons in the bone and its organic matrix are progressing in parallel. Therefore, having a combination of MRI techniques to assess water and organic matrix, plus bone minerals, would be very appealing. Such techniques will enable a comprehensive assessment of bone and surrounding soft tissues in one MRI session that significantly benefits both patients and physicians.

5. Conclusion

Cones 3D UTE-MRI QSM was employed for the first time to investigate the correlation of QSM with BMD in human tibial cortical bone specimens. Cones 3D UTE-MRI previously demonstrated a faster scanning process compared with other 3D UTE-QSM methods. Presented average Cones 3D UTE-MRI QSM values in bone specimens showed significantly strong correlations with their average BMD and porosity. When combining all datasets together, QSM estimations showed significant moderate to strong correlation with BMD, likely indicating lower intraspecimen correlation between QSM and BMD. This study highlighted Cones 3D UTE-MRI QSM technique as a useful method to assess intracortical BMD, which may be used in future clinical studies to avoid ionizing radiation.

Supplementary Material

Refer to Web version on PubMed Central for supplementary material.

Acknowledgements

The authors acknowledge grant support from NIH (1R21AR073496, R01AR068987, and 1R01AR062581–01A1) and VA Clinical Science and Rehabilitation R&D (I01CX001388 and I01RX002604).

Abbreviations:

MR	magnetic resonance
MRI	magnetic resonance imaging

3D	three-dimensional
3D- UTE	three-dimensional ultrashort echo time imaging
RF	radio frequency
FOV	field of view
MT	magnetization transfer
ROI	region of interest
TE	echo time
TR	repetition time
CT	computed tomography
μCT	micro-computed tomography
QSM	quantitative susceptibility mapping
FA	flip angle
BMD	bone mineral density
PBS	phosphate buffered saline
DEXA	dual-energy X-ray absorptiometry
IDEAL	iterative decomposition of water and fat with echo symmetry and least-squires estimation
CSSR	chemical shift species-specific R2* signal
PDF	Projection onto Dipole Fields

References

[1]. Manhard MK, Nyman JS, Does MD. Advances in imaging approaches to fracture risk evaluation. Transl Res 2017;181:1–14. doi:10.1016/j.trsl.2016.09.006. [PubMed: 27816505]

[2]. Moser E, Rejnmark L, Sikjaer T, Mosekilde L, Amstrup AK, Jakobsen NFB. Association between bone indices assessed by DXA, HR-pQCT and QCT scans in post-menopausal women. J Bone Miner Metab 2015;34:638–45. doi:10.1007/s00774-015-0708-9. [PubMed: 26293682]

[3]. Du J, Bydder GM. Qualitative and quantitative ultrashort-TE MRI of cortical bone. NMR Biomed 2013;26:489–506. doi:10.1002/nbm.2906. [PubMed: 23280581]

[4]. Chang EY, Du J, Chung CB. UTE imaging in the musculoskeletal system. J Magn Reson Imaging 2015;41:870–83. doi:10.1002/jmri.24713. [PubMed: 25045018]

[5]. Wehrli FW. Magnetic resonance of calcified tissues. J Magn Reson 2013;229:35–48. doi:10.1016/j.jmr.2012.12.011. [PubMed: 23414678]

[6]. Dimov AV, Liu Z, Spincemaille P, Prince MR, Du J, Wang Y. Bone quantitative susceptibility mapping using a chemical species-specific R2* signal model with ultrashort and conventional echo data. Magn Reson Med 2017;79:121–8. doi:10.1002/mrm.26648. [PubMed: 28261863]

[7]. Barbosa JHO, Santos AC, Tumas V, Liu M, Zheng W, Haacke EM, et al. Quantifying brain iron deposition in patients with Parkinson's disease using quantitative susceptibility mapping, R2 and

R2*. Magn Reson Imaging 2015;33:559–65. doi:10.1016/j.mri.2015.02.021. [PubMed: 25721997]

[8]. Acosta-Cabronero J, Betts MJ, Cardenas-Blanco A, Yang S, Nestor PJ. In Vivo MRI Mapping of Brain Iron Deposition across the Adult Lifespan. J Neurosci 2016;36:364–74. doi:10.1523/JNEUROSCI.1907-15.2016. [PubMed: 26758829]

[9]. Chen W, Zhu W, Kovanlikaya I, Kovanlikaya A, Liu T, Wang S, et al. Intracranial calcifications and hemorrhages: characterization with quantitative susceptibility mapping. Radiology 2014;270:496–505. doi:10.1148/radiol.13122640. [PubMed: 24126366]

[10]. Straub S, Laun FB, Emmerich J, Jobke B, Hauswald H, Katayama S, et al. Potential of quantitative susceptibility mapping for detection of prostatic calcifications. J Magn Reson Imaging 2017;45:889–98. doi:10.1002/jmri.25385. [PubMed: 27418017]

[11]. Wisnieff C, Ramanan S, Olesik J, Gauthier S, Wang Y, Pitt D. Quantitative susceptibility mapping (QSM) of white matter multiple sclerosis lesions: Interpreting positive susceptibility and the presence of iron. Magn Reson Med 2015;74:564–70. doi:10.1002/mrm.25420. [PubMed: 25137340]

[12]. Chen W, Gauthier SA, Gupta A, Comunale J, Liu T, Wang S, et al. Quantitative Susceptibility Mapping of Multiple Sclerosis Lesions at Various Ages. Radiology 2014;271:183–92. doi:10.1148/radiol.13130353. [PubMed: 24475808]

[13]. Langkammer C, Liu T, Khalil M, Enzinger C, Jehna M, Fuchs S, et al. Quantitative Susceptibility Mapping in Multiple Sclerosis. Radiology 2013;267:551–9. doi:10.1148/radiol.12120707. [PubMed: 23315661]

[14]. Wen Y, Nguyen TD, Liu Z, Spincemaille P, Zhou D, Dimov AV., et al. Cardiac quantitative susceptibility mapping (QSM) for heart chamber oxygenation. Magn Reson Med 2017;1552:1545–52. doi:10.1002/mrm.26808.

[15]. Fan AP, Bilgic B, Gagnon L, Witzel T, Bhat H, Rosen BR, et al. Quantitative oxygenation venography from MRI phase. Magn Reson Med 2014;72:149–59. doi:10.1002/mrm.24918. [PubMed: 24006229]

[16]. Zhang J, Liu T, Gupta A, Spincemaille P, Nguyen TD, Wang Y. Quantitative mapping of cerebral metabolic rate of oxygen (CMRO 2) using quantitative susceptibility mapping (QSM). Magn Reson Med 2015;74:945–52. doi:10.1002/mrm.25463. [PubMed: 25263499]

[17]. Xu B, Liu T, Spincemaille P, Prince M, Wang Y. Flow compensated quantitative susceptibility mapping for venous oxygenation imaging. Magn Reson Med 2014;72:438–45. doi:10.1002/mrm.24937. [PubMed: 24006187]

[18]. De Rochefort L, Liu T, Kressler B, Liu J, Spincemaille P, Lebon V, et al. Quantitative susceptibility map reconstruction from MR phase data using bayesian regularization: Validation and application to brain imaging. Magn Reson Med 2010;63:194–206. doi:10.1002/mrm.22187. [PubMed: 19953507]

[19]. Wang Y, Liu T. Quantitative susceptibility mapping (QSM): Decoding MRI data for a tissue magnetic biomarker. Magn Reson Med 2015;73:82–101. doi:10.1002/mrm.25358. [PubMed: 25044035]

[20]. Chen Y, Guo Y, Feng Y, Zhang X, Mei Y, Zhang X. Bone susceptibility mapping with MRI is an alternative and reliable biomarker of osteoporosis in postmenopausal women. Eur Radiol 2018;28:5027–34. doi:10.1007/s00330-018-5419-x. [PubMed: 29948078]

[21]. Diefenbach Maximilian N.Meineke J, Ruschke S, Baum T, Gersing A, Karampinos DC. On the sensitivity of quantitative susceptibility mapping for measuring trabecular bone density. Magn Reson Med 2018;81:1739–54. doi:10.1002/mrm.27531. [PubMed: 30265769]

[22]. Rajapakse CS, Bashoor-Zadeh M, Li C, Sun W, Wright AC, Wehrli FW. Volumetric Cortical Bone Porosity Assessment with MR Imaging: Validation and Clinical Feasibility. Radiology 2015;276:526–35. doi:10.1148/radiol.15141850. [PubMed: 26203710]

[23]. Seifert AC, Wehrli FW. Solid-State Quantitative 1H and 31P MRI of Cortical Bone in Humans. Curr Osteoporos Rep 2016:1–10. doi:10.1007/s11914-016-0307-2. [PubMed: 26861807]

[24]. Granke M, Does MD, Nyman JS. The Role of Water Compartments in the Material Properties of Cortical Bone. Calcif Tissue Int 2015;97:292–307. doi:10.1007/s00223-015-9977-5. [PubMed: 25783011]

[25]. Nyman JS, Ni Q, Nicolella DP, Wang X. Measurements of mobile and bound water by nuclear magnetic resonance correlate with mechanical properties of bone. Bone 2008;42:193–9. doi: 10.1016/j.bone.2007.09.049. [PubMed: 17964874]

[26]. Du J, Hermida JC, Diaz E, Corbeil J, Znamirowski R, D'Lima DD, et al. Assessment of cortical bone with clinical and ultrashort echo time sequences. Magn Reson Med 2013;70:697–704. doi: 10.1002/mrm.24497. [PubMed: 23001864]

[27]. Manhard MK, Uppuganti S, Granke M, Gochberg DF, Nyman JS, Does MD. MRI-derived bound and pore water concentrations as predictors of fracture resistance. Bone 2016;87:1–10. doi: 10.1016/j.bone.2016.03.007. [PubMed: 26993059]

[28]. Diaz E, Chung CB, Bae WC, Statum S, Znamirowski R, Bydder GM, et al. Ultrashort echo time spectroscopic imaging (UTESI): an efficient method for quantifying bound and free water. NMR Biomed 2012;25:161–8. doi:10.1002/nbm.1728. [PubMed: 21766381]

[29]. Du J, Carl M, Bydder M, Takahashi A, Chung CB, Bydder GM. Qualitative and quantitative ultrashort echo time (UTE) imaging of cortical bone. J Magn Reson 2010;207:304–11. doi: 10.1016/j.jmr.2010.09.013. [PubMed: 20980179]

[30]. Chen J, Chang EY, Carl M, Ma Y, Shao H, Chen B, et al. Measurement of bound and pore water T1 relaxation times in cortical bone using three-dimensional ultrashort echo time cones sequences. Magn Reson Med 2016;77:2136–45. doi:10.1002/mrm.26292. [PubMed: 27263994]

[31]. Du J, Diaz E, Carl M, Bae WC, Chung CB, Bydder GM. Ultrashort echo time imaging with bicomponent analysis. Magn Reson Med 2012;67:645–9. doi:10.1002/mrm.23047. [PubMed: 22034242]

[32]. Li C, Magland JF, Rad HS, Song HK, Wehrli FW. Comparison of optimized soft-tissue suppression schemes for ultrashort echo time MRI. Magn Reson Med 2011;68:680–9. doi: 10.1002/mrm.23267. [PubMed: 22161636]

[33]. Abbasi-Rad S, Saligheh Rad H. Quantification of Human Cortical Bone Bound and Free Water in Vivo with Ultrashort Echo Time MR Imaging: A Model-based Approach. Radiology 2017;000:160780. doi:10.1148/radiol.2016160780.

[34]. Gurney PT, Hargreaves BA, Nishimura DG. Design and analysis of a practical 3D cones trajectory. Magn Reson Med 2006;55:575–82. doi:10.1002/mrm.20796. [PubMed: 16450366]

[35]. Carl M, Bydder GM, Du J. UTE imaging with simultaneous water and fat signal suppression using a time-efficient multispoke inversion recovery pulse sequence. Magn Reson Med 2015;76:577–82. doi:10.1002/mrm.25823. [PubMed: 26309221]

[36]. Ma Y, Zhu Y, Lu X, Carl M, Chang EY, Du J. Short T 2 imaging using a 3D double adiabatic inversion recovery prepared ultrashort echo time cones (3D DIR-UTE-Cones) sequence. Magn Reson Med 2017;00:1–9. doi:10.1002/mrm.26908.

[37]. Du J, Bydder M, Takahashi AM, Carl M, Chung CB, Bydder GM. Short T2 contrast with three-dimensional ultrashort echo time imaging. Magn Reson Imaging 2011;29:470–82. doi:10.1016/j.mri.2010.11.003. [PubMed: 21440400]

[38]. Wansapura JP, Daniel BL, Pauly J, Butts K. Temperature mapping of frozen tissue using eddy current compensated half excitation RF pulses. Magn Reson Med 2001;46:985–92. doi:10.1002/mrm.1285. [PubMed: 11675651]

[39]. Hong W, He Q, Fan S, Carl M, Shao H, Chen J, et al. Imaging and quantification of iron-oxide nanoparticles (IONP) using MP-RAGE and UTE based sequences. Magn Reson Med 2016;78:226–32. doi:10.1002/mrm.26371. [PubMed: 27495266]

[40]. Chen J, Carl M, Ma Y, Shao H, Lu X, Chen B, et al. Fast volumetric imaging of bound and pore water in cortical bone using three-dimensional ultrashort-TE (UTE) and inversion recovery UTE sequences. NMR Biomed 2016;29:1373–80. doi:10.1002/nbm.3579. [PubMed: 27496335]

[41]. Ma Y, Carl M, Shao H, Tadros AS, Chang EY, Du J. Three-dimensional ultrashort echo time cones T 1ρ (3D UTE-cones-T 1ρ) imaging. NMR Biomed 2017;30:e3709. doi:10.1002/nbm.3709.

[42]. Lu X, Ma Y, Chang EY, He Q, Searleman A, von Drygalski A, et al. Simultaneous quantitative susceptibility mapping (QSM) and R2* for high iron concentration quantification with 3D ultrashort echo time sequences: An echo dependence study. Magn Reson Med 2018;00:0–7. doi: 10.1002/mrm.27062.

[43]. Lu X, Jang H, Ma Y, Jerban S, Chang EY, Du J. Ultrashort Echo Time Quantitative Susceptibility Mapping (UTE-QSM) of Highly Concentrated Magnetic Nanoparticles: A Comparison Study about Different Sampling Strategies. Molecules 2019;24:1143. doi:10.3390/molecules24061143.

[44]. Jang H, Lu X, Carl M, Searleman AC, Jerban S, Ma Y, et al. True phase quantitative susceptibility mapping using continuous single-point imaging: a feasibility study. Magn Reson Med 2018:1–8. doi:10.1002/mrm.27515.

[45]. Cusack R, Papadakis N. New robust 3-D phase unwrapping algorithms: Application to magnetic field mapping and undistorting echoplanar images. Neuroimage 2002;16:754–64. doi:10.1006/nimg.2002.1092. [PubMed: 12169259]

[46]. Reeder SB, Wen Z, Yu H, Pineda AR, Gold GE, Markl M, et al. Multicoil Dixon Chemical Species Separation with an Iterative Least-Squares Estimation Method. Magn Reson Med 2004;51:35–45. doi:10.1002/mrm.10675. [PubMed: 14705043]

[47]. Yu H, McKenzie CA, Shimakawa A, Vu AT, Brau ACS, Pineda AR, et al. Multiecho reconstruction for simultaneous water-fat decomposition and T2* estimation. J Magn Reson Imaging 2007;26:1153–61. doi:10.1002/jmri.21090. [PubMed: 17896369]

[48]. Yu H, Shimakawa A, McKenzie CA, Brodsky E, Brittain JH, Reeder SB. Multiecho water-fat separation and simultaneous R*2 estimation with multifrequency fat spectrum modeling. Magn Reson Med 2008;60:1122–34. doi:10.1002/mrm.21737. [PubMed: 18956464]

[49]. Liu T, Khalidov I, de Rochefort L, Spincemaille P, Liu J, Tsiouris AJ, et al. A novel background field removal method for MRI using projection onto dipole fields (PDF). NMR Biomed 2011;24:1129–36. doi:10.1002/nbm.1670. [PubMed: 21387445]

[50]. De Rochefort L, Brown R, Prince MRR, Wang Y. Quantitative MR susceptibility mapping using piece-wise constant regularized inversion of the magnetic field. Magn Reson Med 2008;60:1003–9. doi:10.1002/mrm.21710. [PubMed: 18816834]

[51]. Jerban S, Ma Y, Nazaran A, Dorthe EW, Cory E, Carl M, et al. Detecting stress injury (fatigue fracture) in fibular cortical bone using quantitative ultrashort echo time-magnetization transfer (UTE-MT): An ex vivo study. NMR Biomed 2018;31:e3994. doi:10.1002/nbm.3994. [PubMed: 30059184]

[52]. Kijowski R, Choi J, Shinki K, Del Rio AM, De Smet A. Validation of MRI classification system for tibial stress injuries. Am J Roentgenol 2012;198:878–84. doi:10.2214/AJR.11.6826. [PubMed: 22451555]

[53]. Bae WC, Chen PC, Chung CB, Masuda K, D'Lima D, Du J. Quantitative ultrashort echo time (UTE) MRI of human cortical bone: Correlation with porosity and biomechanical properties. J Bone Miner Res 2012;27:848–57. doi:10.1002/jbmr.1535. [PubMed: 22190232]

[54]. Lu X, Jerban S, Wan L, Ma Y, Jang H, Le N, et al. Three Dimensional Ultrashort Echo Time Imaging with Tri-component Analysis for Human Cortical Bone. Magn Reson Med 2019;00:1–8. doi:10.1002/mrm.27718.

[55]. Manhard MK, Horch RA, Harkins KD, Gochberg DF, Nyman JS, Does MD. Validation of quantitative bound- and pore-water imaging in cortical bone. Magn Reson Med 2014;71:2166–71. doi:10.1002/mrm.24870. [PubMed: 23878027]

[56]. Li C, Seifert AC, Rad HS, Bhagat Y a, Rajapakse CS, Sun W, et al. Cortical Bone Water Concentration: Dependence of MR Imaging Measures on Age and Pore Volume Fraction. Radiology 2014;272:796–806. doi:10.1148/radiol.14132585. [PubMed: 24814179]

[57]. Granke M, Makowski AJ, Uppuganti S, Does MD, Nyman JS. Identifying Novel Clinical Surrogates to Assess Human Bone Fracture Toughness. J Bone Miner Res 2015;30:1290–300. doi:10.1002/jbmr.2452. [PubMed: 25639628]

[58]. Rad HS, Lam SCB, Magland JF, Ong H, Li C, Song HK, et al. Quantifying cortical bone water in vivo by three-dimensional ultra-short echo-time MRI. NMR Biomed 2011;24:855–64. doi:10.1002/nbm.1631. [PubMed: 21274960]

[59]. Chang EY, Bae WC, Shao H, Biswas R, Li S, Chen J, et al. Ultrashort echo time magnetization transfer (UTE-MT) imaging of cortical bone. NMR Biomed 2015;28:873–80. doi:10.1002/nbm.3316. [PubMed: 25981914]

[60]. Jerban S, Ma Y, Wan L, Searleman AC, Jang H, Sah RL, et al. Collagen proton fraction from ultrashort echo time magnetization transfer (UTE-MT) MRI modelling correlates significantly

with cortical bone porosity measured with micro-computed tomography (μCT). NMR Biomed 2019;32:1–10. doi:10.1002/nbm.4045.

[61]. Jerban S, Ma Y, Wong JH, Nazaran A, Searleman A, Wan L, et al. Ultrashort echo time magnetic resonance imaging (UTE-MRI) of cortical bone correlates well with histomorphometric assessment of bone microstructure. Bone 2019;123:8–17. doi:10.1016/j.bone.2019.03.013. [PubMed: 30877070]

[62]. Han M, Scott SJ, Ozhinsky E, Salgaonakar VA, Jones PD, Larson PEZ, et al. Assessing temperature changes in cortical bone using variable flip-angle ultrashort echo-time MRI. AIP Conf Proc 2017;1821. doi:10.1063/1.4977625.

[63]. Jerban S, Szeverenyi N, Ma Y, Guo T, Namiranian B, To S, et al. Ultrashort echo time MRI (UTE-MRI) quantifications of cortical bone varied significantly at body temperature compared with room temperature. Investig Magn Reson Imaging 2019;In Press.

[64]. Wan L, Zhao W, Ma Y, Jerban S, Searleman AC, Carl M, et al. Fast quantitative three-dimensional ultrashort echo time (UTE) magnetic resonance imaging of cortical bone using extended cones sampling. Magn Reson Med 2019. doi:10.1002/mrm.27715.

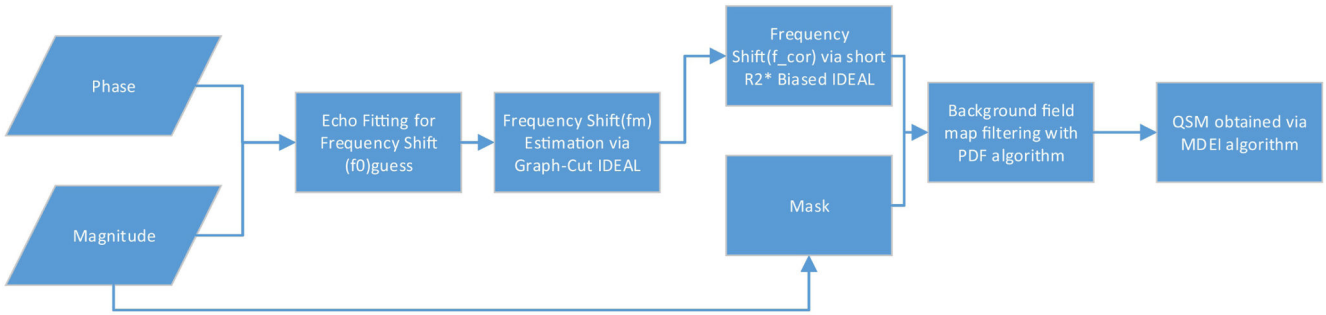

Figure 1:
QSM measurement flowchart using the magnitude and phase images.

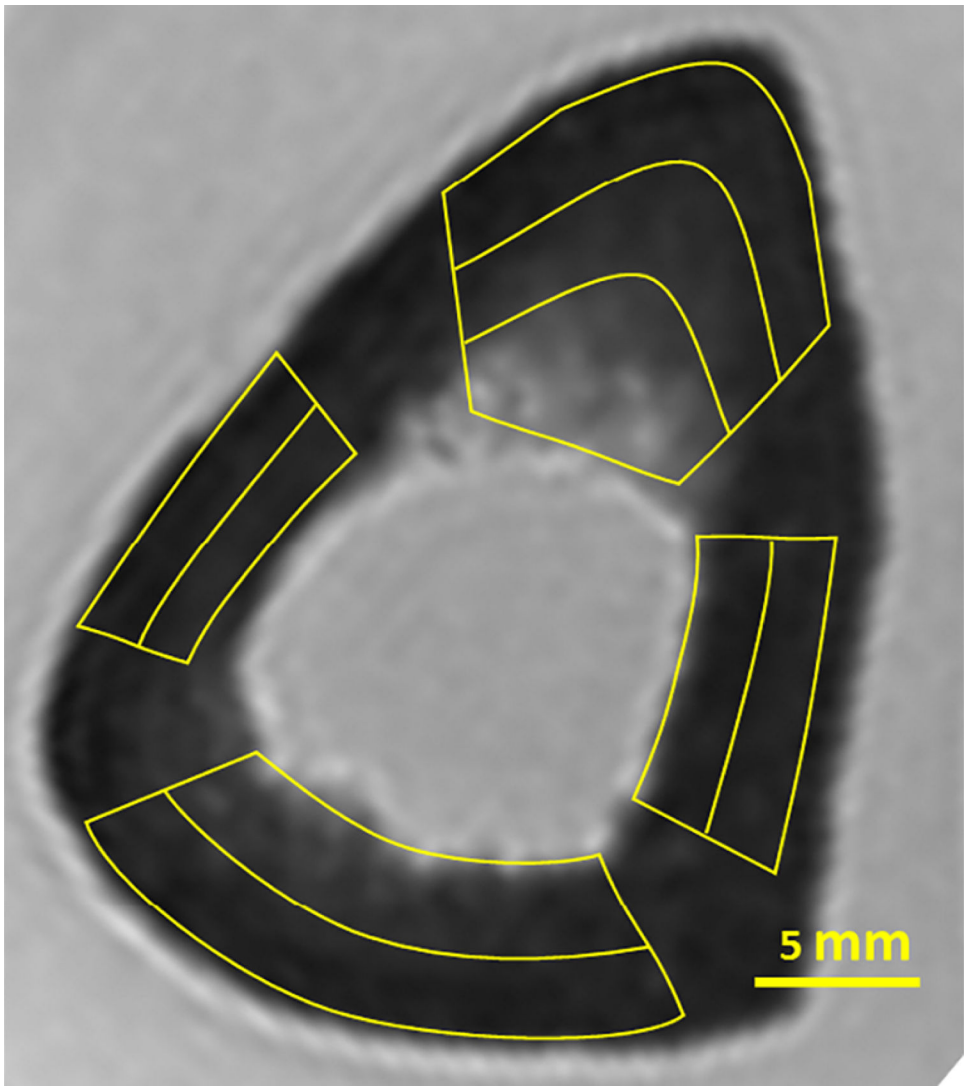

Figure 2:
Schematics of nine selected ROIs on Cones 3D UTE-MRI (TE=0.032ms) image (0.5×0.5×2mm voxel size) of a representative tibial midshaft cortical bone (45-year-old female).

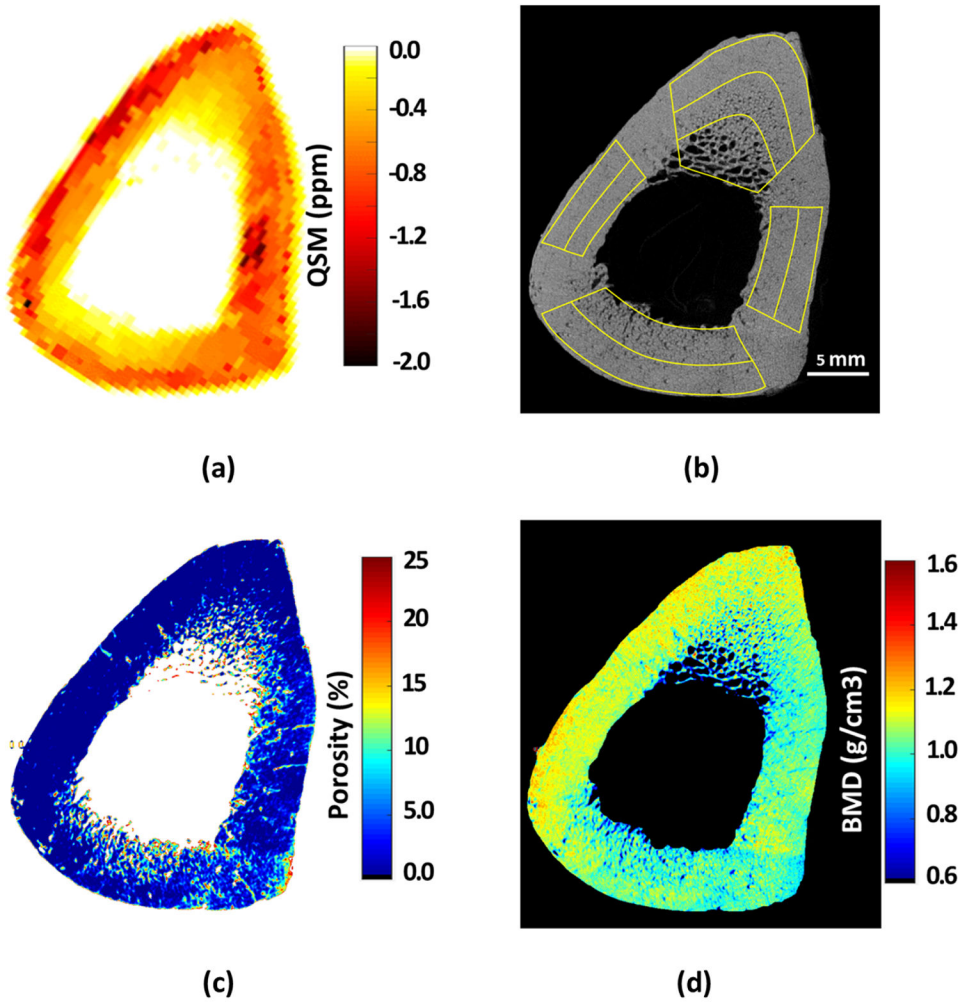

Figure 3:
(a) Quantitative susceptibility map (QSM) using Cones 3D UTE-MRI scans (0.5×0.5×2mm voxel size) of a representative tibial midshaft cortical bone (45-year-old female), (b) one representative μCT slice at 9 μm isotropic voxel size, (c) μCT-based porosity, and (d) bone mineral density (BMD) maps of the same representative tibial bone specimen. Local maxima in the QSM map clearly correspond to the regions of high BMD and low porosity in μCT-based maps.

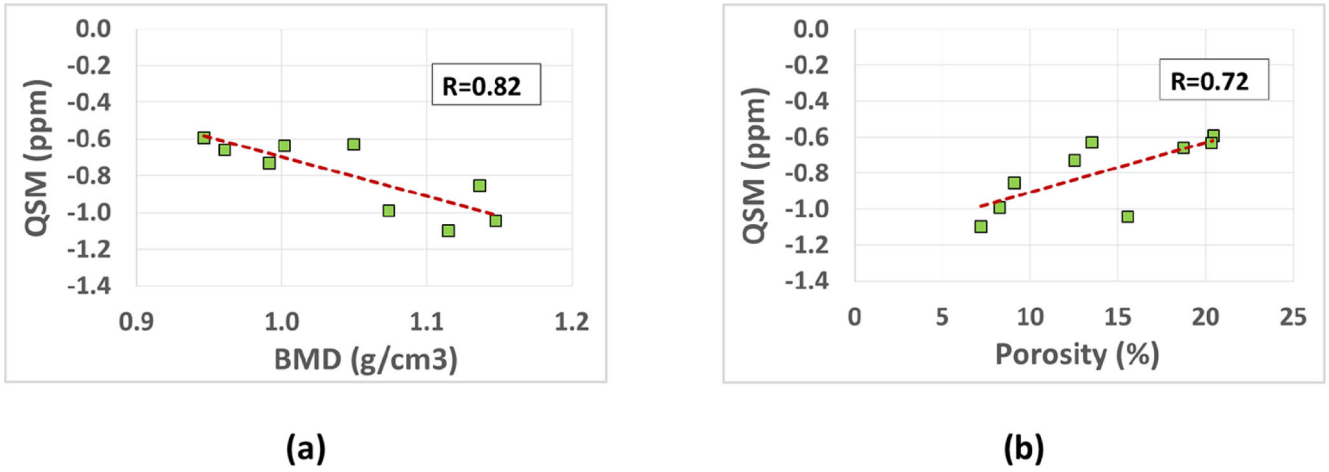

Figure 4:

Scatter plot and linear regressions of average quantitative susceptibility mapping (QSM) of the nine studied bone specimens on their (a) bone mineral density, BMD, and on (b) bone porosity.

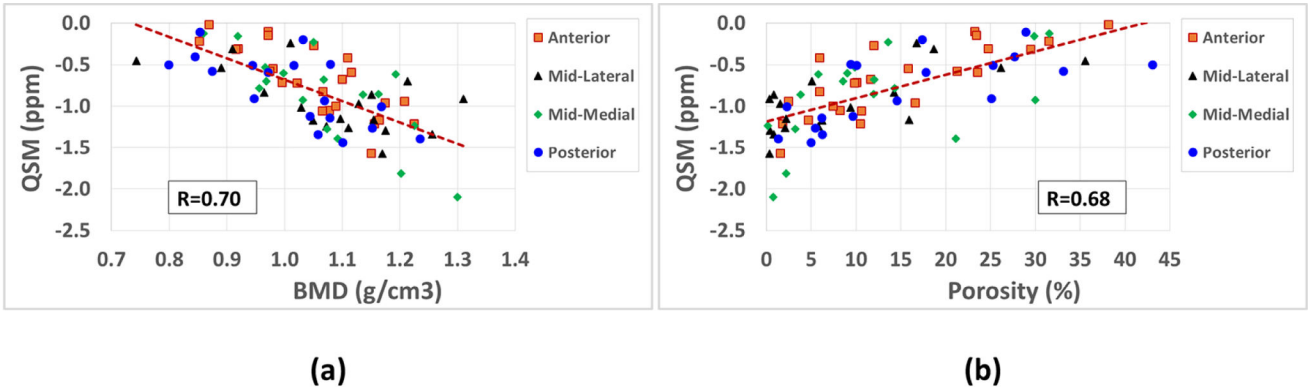

(a) (b)

Figure 5:

Scatter plot and linear regressions of QSM on (a) BMD, and on (b) bone porosity. Correlation coefficients were lower when combining all data points together. Significance levels for these correlations were below 0.01, as measured using non-parametric bootstrap (with resampling by specimen) to adjust for within-specimen dependence. Anterior, mid-lateral, mid-medial, and posterior data points are illustrated with markers, where no obvious differences were found between bone sites in the limited number of studied specimens.

Table 1:

Donor information, average, and standard deviation values of QSM, BMD, and bone porosity measures in nine studied bone specimens.

	Gender	Age	Porosity (%)	BMD (g/cm3)	QSM (ppm)
Sample 1	F	86	20.4±6.1	0.95±0.08	−0.59±0.41
Sample 2	F	95	18.7±10.7	0.96±0.08	−0.65±0.34
Sample 3	F	90	12.5±10.3	0.99±0.11	−0.73±0.32
Sample 4	M	73	7.2±8.4	1.11±0.11	−1.09±0.44
Sample 5	M	71	13.5±8.3	1.05±0.08	−0.62±0.42
Sample 6	M	53	20.3±14.4	1.00±0.14	−0.63±0.49
Sample 7	F	49	9.1±8.6	1.14±0.11	−0.85±0.47
Sample 8	F	45	8.2±9.1	1.07±0.08	−0.99±0.36
Sample 9	F	38	15.5±8.8	1.15±0.06	−1.04±0.29

Table 2:

Pearson's correlations, 95% significant intervals, and p values between UTE-MRI QSM and μCT-based results (BMD and porosity) when considering all data points together (77 ROIs). Significance for all correlations was assessed using non-parametric bootstrap (with resampling by specimen) to adjust for within-specimen dependence.

	BMD	Bone porosity
QSM	**−0.70**	**0.68**
	[−0.80, −0.54]	[0.50, 0.76]
	p<0.01	p<0.01